Chapter 5

Study of Sunspot Umbral Oscillation as Observed by Goode Solar Telescope (GST) at Big Bear Solar Observatory

Sunspots are the strong concentrations of the magnetic fields that appear at photosphere of the Sun and consists od central umbra and outer penumbra. In this chapter, we study the solar chromospheric oscillations above umbra using intensity oscillations seen at the core and the wings of the Hα line, and the Doppler velocity estimated by the Hα line profiles observed by the Visible Imaging Spectrometer (VIS) at Goode Solar Telescope (GST) commissioned at Big Bear Solar Observatory (BBSO). We analyse the periodicities in intensity and Doppler velocity time-series derived from various chosen locations within sunspot umbra using wavelet analysis methods and a general noise model (power law + constant). Our results demonstrate the dominance of the 3-minute period throughout the Doppler velocity oscillations corresponding to the Hα line and in all the intensity time-series derived from different wavelength of the Hα absorption line. In order

to identify different wave modes, we estimate the phase difference using cross wavelet analysis between the intensity time-series (e.g., Hα line core, Hα±0.2 Å, Hα±0.4 Å, and Hα±0.6 Å) and the Doppler velocity oscillations of the Hα line as derived from multitude location in the sunspot umbra. The statistical distribution of the phase differences shows that there are waves travelling both upward and downward in the chromosphere, suggesting that 3 min umbral oscillations are most likely the results of resonant modes inside sunspots.

5.1 Introduction

Sunspot oscillations have been extensively investigated over decades (e.g., Beckers and Tallant, 1969; Bogdan, 2000; Bogdan and Judge, 2006; Jess et al., 2015, 2020; Khomenko and Collados, 2015, and references cited therein). These studies help us comprehending on the seismology of the sunspots (e.g., Felipe et al., 2020; Sych and Nakariakov, 2014; Zhugzhda, 2008, and references cited therein). Furthermore, these investigations of the sunspot oscillations are considered as the primary source of upward propagating waves in the corona. (e.g., Chae et al., 2017; Hou et al., 2018; Jess et al., 2012; Krishna Prasad et al., 2017; Verwichte et al., 2010; Yuan et al., 2014). Sunspots exhibit regular oscillations in both intensity and velocity, occurring in both their dark centers (umbrae) and brighter outer regions (penumbrae) (e.g., Khomenko and Collados, 2015, and references cited therein). Sunspot waves are broadly categorised in three types, namely, running penumbral waves, chromospheric umbral oscillations, and photospheric umbral oscillations (e.g., Bellot Rubio et al., 2000; Lites, 1992). The 5 min oscillations dominate the phtospheric umbral waves, along with the presence of 3 min power in the power spectrum (e.g., Thomas et al., 1982), whereas 3 min oscillations dominate the chromospheric umbral waves (Lites, 1984). Running penumbral waves have a periodicity of few minutes and are detected in

the chromospheric penumbra as outward propagating oscillations (e.g., Christopoulou et al., 2000; Jess et al., 2013). Sunspot waves are slow magnetoacoustic waves that travel along the magnetic field lines (e.g., Centeno et al., 2006b; Jess et al., 2013). These upward propagating waves became the shocks owing to the steepening and dispersed their energy that may operate as a source of the energy to heat the chromosphere or corona (e.g., Centeno et al., 2006b; Tian et al., 2014a). Kanoh et al. (2016) estimated the energy flow at two different atmospheric heights, i.e., photosphere and lower transition region above a sunspot. They found that the difference in energy flux is enough to heat the solar chromosphere. However, they predict a flux of 10^4 erg $cm^{-2}s^{-1}$ in the lower transition region, which cannot heat the solar corona. Therefore, another energy source is needed for heating the solar corona (e.g., Anderson and Athay, 1989; Mein and Schmieder, 1981).

At the photospheric level, two distinct types of oscillations have been identified, namely, the 5 min waves driven by the specific modes of vibration (p-modes) and 3 min waves representing the sunspot's natural resonance (e.g., Beckers and Schultz, 1972; Giovanelli, 1972; Khomenko and Collados, 2015). These oscillations signifies how much acoustic energy is created by the oscillations beneath the solar surface. Tn the photosphere, these five-minute oscillations are more pronounced than the three-minute oscillations. While, in the chromosphere and transition region, they are hardly visible and their amplitudes are declined with the height. Propagating waves having lower frequency ,i.e., less than 5 mHz may reflctec back from the upper phostosphere, while waves with higher frequencies keep traveling up to the chromosphere. In the chromosphere, the time taken for the oscillations within a sunspot umbra is usually less than three minutes. Moving outward from the center of the sunspot (e.g., Bogdan and Judge, 2006), these oscillation periods gradually becomes longer (e.g., Nagashima et al., 2007).

The 3 min oscillations were first identified as "umbral flashes" and these observations were observed as intensity fluctuations of Ca II K emission from the sunspot umbra (e.g.,

Beckers and Tallant, 1969). These 3 min oscillations have been noted through variations in the brightness of the chromospheric Ca II H and K lines, as well as velocities obtained from He II 10830 Å triplet and the Ca II H and K lines. While these oscillations can be present at different levels in the solar atmosphere, they are mainly seen in the chromosphere, transition region, and corona above sunspot umbra. Numerous studies have shown that three-minute oscillations predominate in the umbra of the chromosphere (e.g., Beckers and Tallant, 1969; Giovanelli, 1972; Gurman, 1987; Lites et al., 1982). Several theories are proposed for 3 min waves in the solar chromosphere. One is resonant cavity model, in which waves are trapped between layers in the solar environment above umbra. This theory is frequently used to explain these observed umbral oscillations (e.g., Gurman, 1987; Lites and Thomas, 1985; Scheuer and Thomas, 1981; Thomas and Scheuer, 1982; Zhugzhda, 2008). Leibacher and Stein (1981) suggested that these oscillations are trapped between a lower boundary, formed by reflection due to the high cut-off frequency at the photosphere's temperature minimum, and an upper boundary caused by the sudden increase in the sound speed in the transition region. Other researchers, however, suggest that waves propagating vertically in a gravitationally stratified medium might be the source of three-minute oscillations in the sunspot umbra (e.g., Cho et al., 2015; Felipe et al., 2010b; Krishna Prasad et al., 2017). Fleck and Schmitz (1991) suggested that these oscillations may be described without the necessity for a chromospheric cavity, due to the resonant activation of the acoustic cut-off frequency mode in such a medium (Felipe et al., 2010a).

The importance of resonances in the photosphere (Chae et al., 2019) and chromosphere of the sunspot umbrae have been the subject of various studies in recent years (e.g., Botha et al., 2011; Felipe, 2019; Snow et al., 2015; Wójcik et al., 2018; Yuan et al., 2016). By considering the temperature fluctuations with height, Zhugzhda (2008) investigated the impact of such an acoustic resonator. In their recent study, Jess et al. (2020) found a strong peak in high frequency power in the He I 10830 Å data. This finding led them to propose

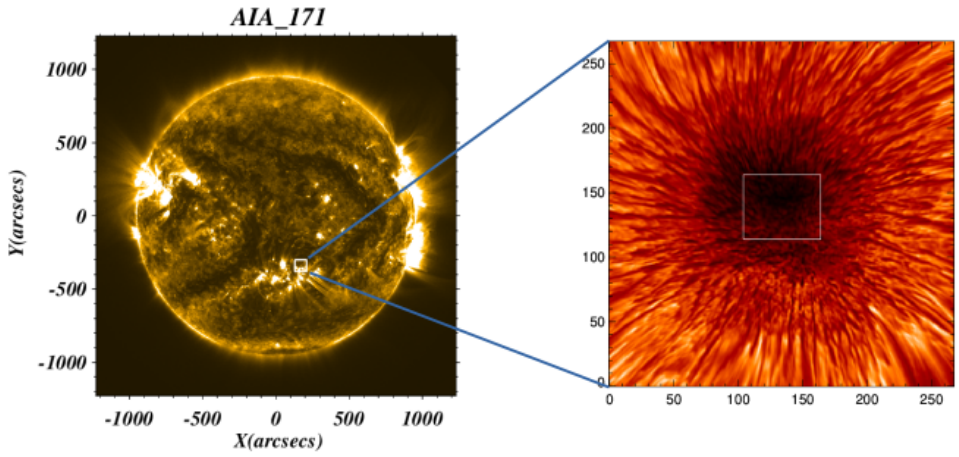

Figure 5.1: The panel on the left presents the full-context image of the sun captured by the Atmospheric Imaging Assembly onboard Solar Dynamics Observatory in the 171 Å filter. A white box indicates the region of interest. The panel on the right shows the field of view in the core of Hα 6563 Å. Pixels within this box were selected for further analysis.

the existence of a resonant cavity above a sunspot. These studies corroborate the existence of an acoustic resonator as a cause of 3 min observed chromospheric oscillations. It is critical to understand that the cutoff frequency still has an influence even with the resonator. In this chapter, we utilize observational data from the BBSO to investigate the origin of three-minute oscillations within a sunspot umbra. Section 5.2 presents comprehensive information regarding the observations and data analysis, while Section 5.3 delves into the methodology employed. Section 5.4 outlines the results obtained from the study. Finally, Section 5.5 interprets the findings and draws conclusions based on the analysis.

5.2 Observations and Data Analysis

We conducted a study on the sunspot AR12384 utilizing observational data acquired from the Visible Imaging Spectrometer (VIS) installed on the Goode Solar Telescope (GST) at the Big Bear Solar Observatory (BBSO) (e.g., Cao et al., 2010). These detailed observations took place on July 14, 2015, spanning a duration of 30 minutes from 17:36

to 18:06 Universal Time (UT). The GST provides a maximum field of view (FOV) of 70″×70″. The GST provides resolutions of 0.2″ at 1.56 μm and 0.06″ at 0.5 μm (e.g., Cao et al., 2010; Yuan et al., 2023). The VIS operates within the wavelength range of 5500 Å to 7000 Å, employing a Fabry-Pérot etalon to generate a narrow bandpass of 0.07 Å across a circular field of view (FOV) measuring 70″ in diameter. The device is capable of recording spectral lines including Hα, Fe I at 6300 Å, and Na I D2 at 5890 Å. For this investigation, the sunspot in the Hα line at 6563 Å was scanned by the VIS at intervals of 0.2 Å, covering the red wing (+1.0 Å) and the blue wing (-1.0 Å). Images of the chromosphere were taken every 19 seconds. To account for air turbulence and capture fine-scale plasma dynamics, speckle imaging methods were employed to recreate every image. The observed region, indicated by the white box overlaid on the AIA filter 171Å image, is depicted in Figure 1. The right panel displays a zoomed-in view in the hα wavelength. In Figure 1b, the dark umbral region is clearly visible, along with the light, bright penumbral region. To process the Hα temporal image data, we applied averaging of spatial area. A 3x3 pixel box was selected, and the values within this box were averaged and stored. Consequently, our data points were reduced by a factor of 9. Figure 1b displays the resulting image obtained after averaging the original data. For the analysis of umbral oscillations, all pixels within the white box were considered. Approximately 3000 pixels were contained within this area. By analyzing this data extensively, we were able to study umbral oscillations statistically. time-series data were extracted for each pixel location for: Hα line core, Hα±0.2 Å, Hα±0.4 Å, and Hα±0.6 Å. We have shown one representative example of time-series for different filters in Figure 5.2. We utilized the wavelet tool to each intensity time-series and compute the significant periods for each filters. Our study involves employing cross-wavelet and phase difference analysis to evaluate the correlation between velocity oscillation and the intensity oscillations corresponding to each filters. Section 5.3 presents the wavelet analysis and cross wavelet analysis in details.

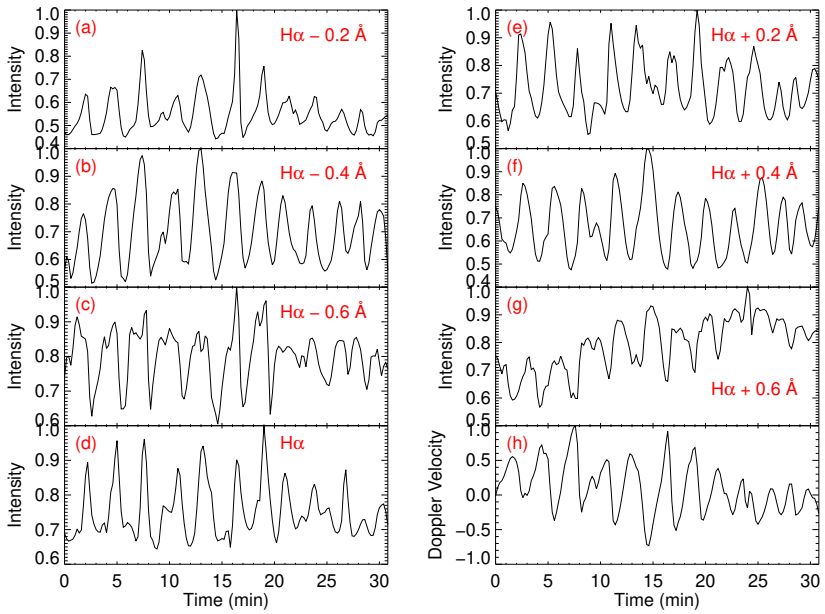

Figure 5.2: Evolution of the intensity over the time for different wavelength, e.g., Hα-0.2 Å, Hα-0.4 Å, Hα-0.6 Å,Hα line core, Hα+0.2 Å, Hα+0.4 Å, Hα+0.6 Å, and Doppler Velocity of Hα line respectively are displayed in panel (a), (b), (c), (d), (e), (f), (g), and (h) respectively. These signals are derived from a pixel from location (x = 119″, y = 159″).

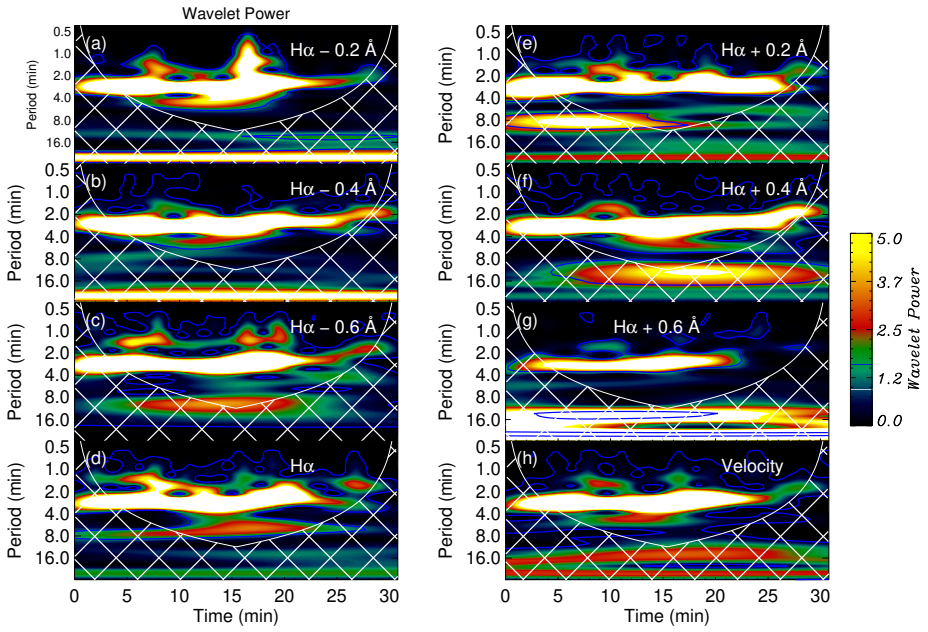

Figure 5.3: Panels (a)-(c) present the wavelet transformation of the intensity time-series in blue wings of Hα filter. Panel (d) shows the wavelet transformation of the intensity time-series from the Hα line core. Panels (e)-(g) display the wavelet transformation for the intensity time-series from the red wings of the Hα. Finally, panel (j) illustrates the wavelet transformation of the Doppler velocity time-series derived from the Hα line profile. These various time-series are shown in Figure 5.2.

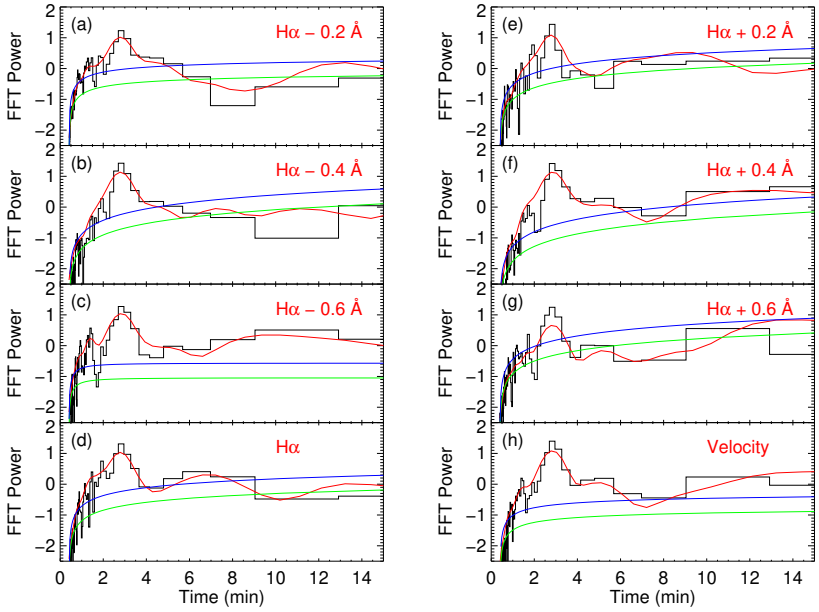

Figure 5.4: In panel (a), the FFT power of Hα-0.2 Å filter intensity time-series is presented by the black curve, while the red curve shows the time-averaged global power of the wavelet spectrum. The power law model is used to compute the fitted model. The fitted model is shown in green color curve. The 95% local significance level is derived from this model and shown in the blue color. Similarly, panels (b) to (g) display the FFT power, global wavelet power, model fit, and 95% local significance level for the intensity time-series of the Hα-0.4 Å, Hα-0.6 Å, Hα line core, Hα+0.2 Å, Hα+0.4 Å, and Hα+0.6 Å, respectively. Panel (h) presents the same for the Doppler velocity time-series.

5.3 Methodology

5.3.1 Wavelet analysis

We used wavelet analysis to find the periodicity in the intensity and velocity time-series. We may find oscillatory powers in the frequency and time domains using this method. The process of wavelet analysis, as described by Torrence and Compo (1998), entails convolving the time-series using a "mother" function. In their work, several mother functions are described, such as the derivative of Gaussian (DOG), Paul, and Morlet. We made use of the Morlet function, which is a plane wave that has a Gaussian function modulating it. The time-series is converted into a 2D complex array using the wavelet transform, and the square of the complex array's absolute value is known as the wavelet power. Following the recommendation of Auchère et al. (2016), we refrained from applying any smoothing prior to conducting the wavelet transform to avoid introducing artificial periodicities. The details of wavelet is already is described in chapter 2. In Figure 5.3, we presented the results of analyzing the different time-series using the wavelet analysis. The "Cone of Influence" (COI) is marked by the white cross-hatched area, where edge effects become pronounced and the power measurements are deemed unreliable. Consequently, we did not use power metrics from the COI in our study. Auchère et al. (2016) have shown that detrending may produce misleading periodicities even if it can be used to eliminate long-period components from the time-series. As a result, we did not detrend the various time-series before using the wavelet technique. We determined 95% local confidence level in order to verify the accuracy of our obtained power and period values. This required modelling the background noise, typically using red and white noise as the models (e.g., Torrence and Compo, 1998). We chose a generic power noise model, defined as a power-law function plus a constant component, as a substitute for these models since we have found that they can occasionally distort the magnitude of the observed power (e.g., Auchère et al., 2016).

We estimated the 95% local confidence level for each time-series by fitting a power law model to the FFT and using the generated background model. A detailed description of this model can be found in our previous work as reported by Sangal et al. (2022, 2024). For the time-series described in Figure 5.2. The Figure 5.4 shows the fitted model (in green) and the 95% local confidence level (in blue). Analysing the dominating oscillations is facilitated by global wavelet power, which is a representation of the time-averaged wavelet power. The global wavelet power for several time-series is shown in Figure 5.4 by the red curve; peaks over the 95% local confidence level denote a considerable power and dominating periods. In Figure 5.3, we overlay 95% local confidence levels on the wavelet power spectra, in contrast to other previous findings that use global wavelet power to identify the dominant period. To extract valid periods from each time-series of Hα, we used this particular criteria, i.e., power must be significant (inside the significant contour) and outside the COI to avoid edge effects. These criteria, which were consistent with our previous work, guaranteed an extraction of the effective period (e.g., Sangal et al., 2022, 2024). After gathering all reliable periods from the wavelet transformations, we produced intensity period histograms for different Hα time-series and the Doppler velocity derived from different location within sunspot umbrae.

5.3.2 Cross-wavelet analysis

In order to determine the correlations and phase differences between two time-series datasets, cross-wavelet analysis is utilised (e.g., Torrence and Compo, 1998). The resultant cross-spectrum indicates places where the time-series share power, while the wavelet coherence indicates regions where the oscillations are synchronised regardless of the common power between the time-series. Wavelet coherence values show the level of synchronisation, and they range from zero (no correlation) to one (highest correlation) (e.g., Torrence and Compo, 1998). The physical properties of oscillations in the umbral

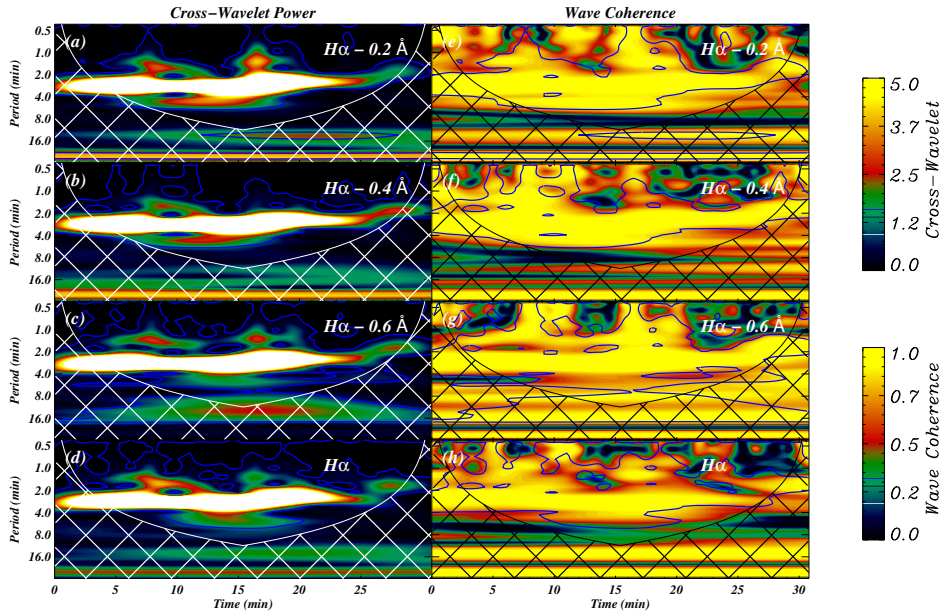

Figure 5.5: Panels (a)-(c) display the cross-wavelet power between intensity oscillations present in the time-series derived from the blue wings of Hα and the Doppler velocity oscillations estimated from the Hα line profile. Panels (e)-(g) illustrate the corresponding wavelet coherence. Panel (d) shows the cross-wavelet power between the Hα core intensity and the Doppler velocity time-series, while panel (h) presents the corresponding wavelet coherence. The blue contours on the plots indicate 95% local significance level calculated using a power-law noise model.

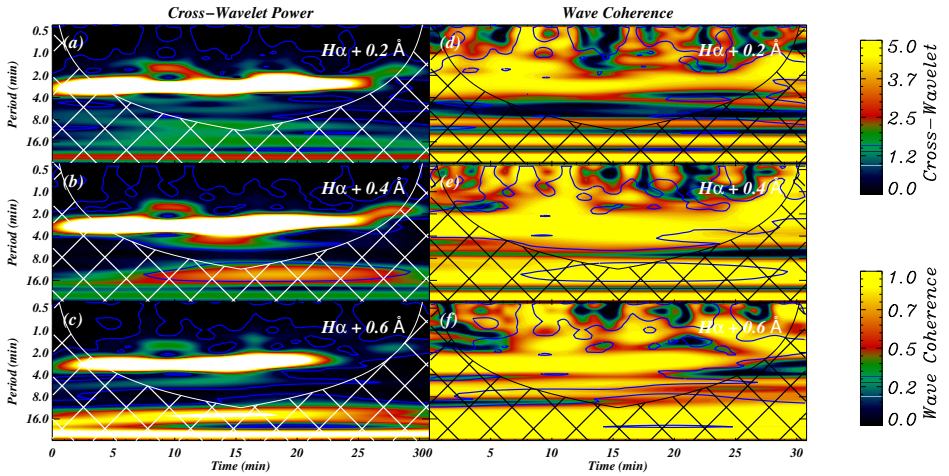

Figure 5.6: Panels (a)-(c) display the cross-wavelet power between the intensity time-series derived from the red wings of Hα and Doppler velocity estimated by the Hα line profile. The related wavelet coherence is shown in Panels (d)–(f).

region can be understood from the analysis of phase differences between the intensity and velocity oscillations (e.g., Torrence and Compo, 1998). We multiplied the wavelet transformation of intensity signals by the complex conjugate of the wavelet of the velocity signals to get the cross wavelet. We squared the absolute magnitude of the resultant cross-wavelet to achieve its power. Figure 5.5 displays the cross-wavelet results between the intensity time-series derived from the Hα blue wings and the Doppler velocity estimated by the Hα line profiles as extracted from the representative location (x = 119″, y = 159″)(panels (a)-(c)), as well as the core intensity of the Hα line and the Doppler velocity (panel (d)). The cross wavelet power is normalised using the product of the power of two time-series to determine the wave coherence. Panels (e)-(g) in Figure 5.5 indicates wave coherence between intensity time-series from the Hα blue wings and the Doppler velocity, whereas panel (g) displays the coherence of the intensity time-series of Hα line core with the Doppler velocity. Figure 5.6 shows a cross-wavelet analysis of the intensity time-series derived from the Hα red wings and Doppler velocity (panels (a)-(c)), as well as the related wave coherence (panels (d)-(f)). Furthermore, by multiplying FFT of the intensity time-series by the complex conjugate of the velocity time-series, the cross Fast Fourier Transforms (FFT) were calculated. We then fitted this with the power law model and calculated the 95% local significance level in the similar manner like we have done in the wavelet analysis. These 95% local significant contour are over plotted in the blue colour in Figures 5.5 and 5.6. Significant power is represented by the power inside these contours. The real and imaginary components of the cross-wavelet power between the intensity of Hα and velocity of Hα line were utilised to compute the phase differences. We used the following particular criteria to choose legitimate phase differences in order to guarantee the accuracy of our findings, i.e., Cross-power needs to be located inside 95% local significance area, In order to prevent edge effects, cross-power inside the Cone of Influence (COI) is eliminated, Only powers with coherence greater than 0.6 were taken

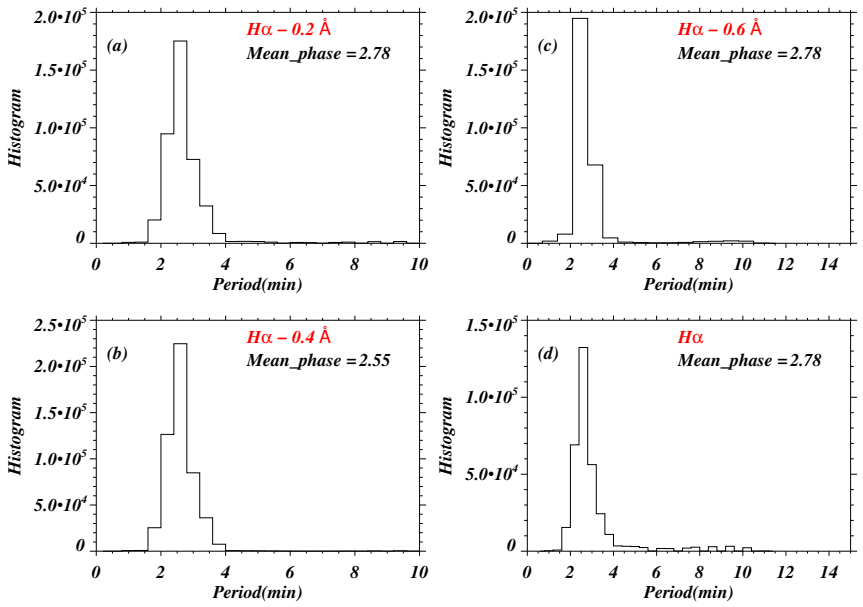

Figure 5.7: Panels (a)-(c) display the histograms of the significant periods from all the chosen locations as estimated analyzing the intensity time-series extracted from the blue wings of Hα, while panel (d) shows the histogram of the significant period for the intensity time-series of the Hα line core. In all panels, the histograms peak at a 3 minute time-scale.

into consideration, according to a wavelet coherence threshold of 0.6. By applying these criteria to every pixel in the umbra (total 3000 pixels), we were able to derive consistent phase differences between Doppler velocity and the intensity of different Hα wavelengths (core, red and blue wings). Using these reliable phase information collected from every pixel, we showed the phase distribution for every wavelength steps in blue wing and core of the Hα line.

5.4 Results

Here, we discuss the results of wavelet and cross-wavelet analyses performed on intensity time-series data from various Hα and Doppler velocity measurements. Figure 5.3 illustrates

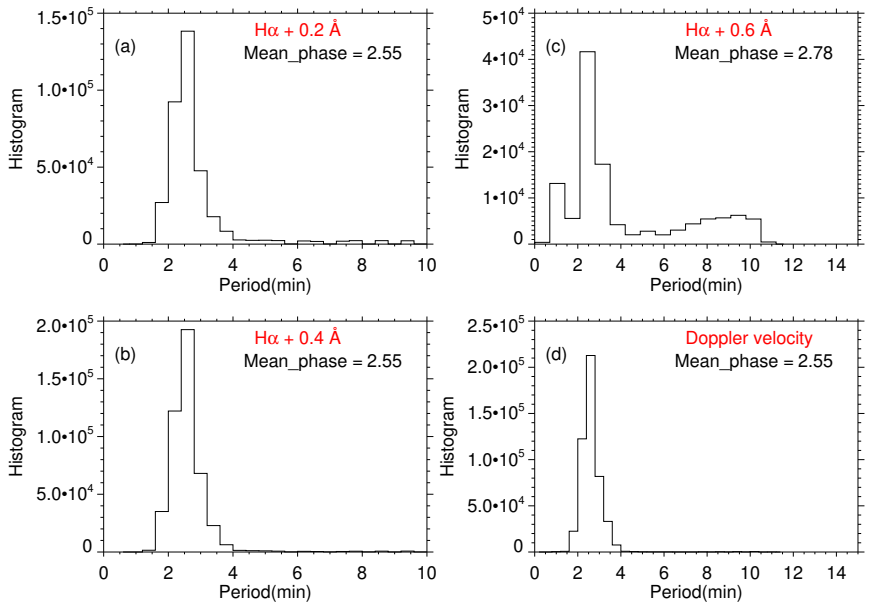

Figure 5.8: In this Figure, we have shown the histogram for the significant periods from al the chosen locations as estimated by analyzing corresponding the intensity time-series as extracted from the red wings of the Hα line. In the red wing as well, the histogram peaks at a 3 minute time scale.

the wavelet analysis results for the intensity time-series of different Hα wavelength in panels (a)-(g) as derived from the representative location (x = 119″, y = 159″). Notably, significant power is observed within a period range of 2-5 minutes across all the panels. The global wavelet power (red plot) depicted in Figure 5.4 further confirms that the power peaks at 3 minutes, indicating a dominant period across all panels (a)-(g). Similarly, panel (h) of Figure 5.3 shows the wavelet analysis results for the Doppler velocity derived using the Hα line profiles, with significant power observed within the 2-5 minute period range and a dominant period of 3 minutes. For representation, we have shown the wavelet analysis for represntation pixel (x = 119″, y = 159″), but we conducted the analyses for all pixels (3000 pixels) within the white box (as depicted in the right panel of Figure 5.1). The intensity time-series of Hα±0.2 Å, Hα±0.4 Å, Hα±0.6 Å, and the Hα line core were subjected to wavelet analysis, while intensity oscillations of Hα±0.8 Åand Hα±1.0 Åwings were omitted from the study due to their formation in the upper photosphere, as our focus is on umbral chromospheric oscillations and also the near photosphere emission may be more optically thick. In the present study, we computed the dominant periodicity based on specific conditions outlined in sub-section 5.3.1, and the reliable significant periods were stored. Histograms of all stored significant periods are presented in Figures 5.7 and 5.8. Panels (a)-(c) of Figure 5.7 display histograms of significant periods corresponding to intensity time-series from all the chosen locations in the blue wings of the Hα line. Panel (d) shows the histogram of significant periods corresponding to the intensity time-series of the Hα core. Similarly, panels (a)-(c) of Figure 5.8 present histograms of significant periods for intensity time-series in the red wings of the Hα line. Panel (d) displays the histogram of the significant periods for velocity signals estimated by the Hα line profiles. We computed the mean period for each case, and the mean phase lies at a time-scale of 3-minutes for all cases, indicating the presence of 3-minute oscillations above the sunspot umbra in the chromospheric region. These 3 min oscillations are commonly recognized as

indicative of slow magnetoacoustic waves (e.g., Bogdan and Judge, 2006). These waves, characterized by their guidance along magnetic field lines, exhibit periodicity of several minutes and travel at the local speed of sound (e.g., Roberts, 2006). Within the umbra of the sunspot, where the plasma has a low plasma-β value, it is widely acknowledged that the slow waves manifest as compressive motions aligned with the magnetic field. These waves may originate as upward-traveling waves from the photosphere, or they may resonate between two reflective boundaries formed by steep temperature gradients between the upper photosphere and the transition region (e.g., Zhugzhda, 2008). In this study, we delve into the nature of these chromospheric oscillations by conducting a phase difference analysis between intensity time-series captured by various Hα wavelengths (core, blue wing, red wing) and velocity time-series estimated from the Hα line profiles.

We explored this by conducting cross-wavelet analysis, which involved examining cross power, wave coherence, and phase differences between the intensity time-series from the Hα line profiles and the Doppler velocity of the Hα line for each pixel within the designated white box (refer to Figure 5.1). In Figure 5.5, panels (a)-(c) indicate noteworthy cross power within the 2-5 minute range, falling within the 95% local significance level. Panels (e)-(g) demonstrate maximum correlation (i.e., 1) corresponding to this significant power. Similarly, significant cross power in the 2-5 minute range is evident in Figure 5.6, with maximum wave coherence observed across all panels (a)-(c). Next, we examined the phase differences between intensity and velocity oscillations to better understand the physical behaviour of sunspot umbral oscillations. We applied cross-wavelet analysis between the intensity time-series of various Hα wavelengths and the Doppler velocity time-series estimated using the Hα line profiles at each pixel locations in the umbra, subsequently calculating the phase differences between intensity and velocity signals. Reliable phase differences were retained for each filter by applying specific conditions outlined in sub-section 5.3.2. The resulting histograms of reliable phase differences for

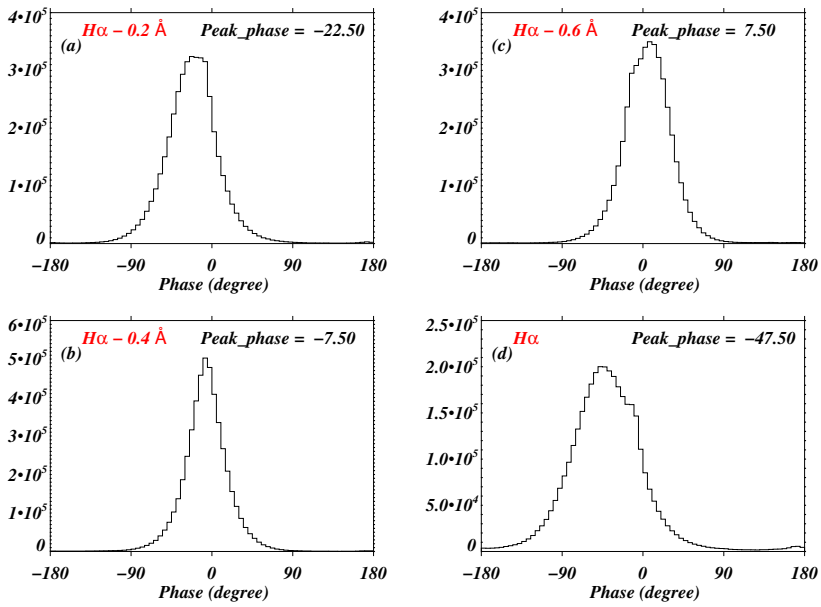

Figure 5.9: Panels (a)-(c) show the histogram of the significant phase differences between the intensity time-series from all chosen locations as extracted from of the blue wings of the Hα and the the velocity signal of the Hα line profile. Panel (d) shows the histogram of phase differences between the intensity time-series of the Hα core and the velocity signals. The peak phase corresponding to each case is mentioned on each panel.

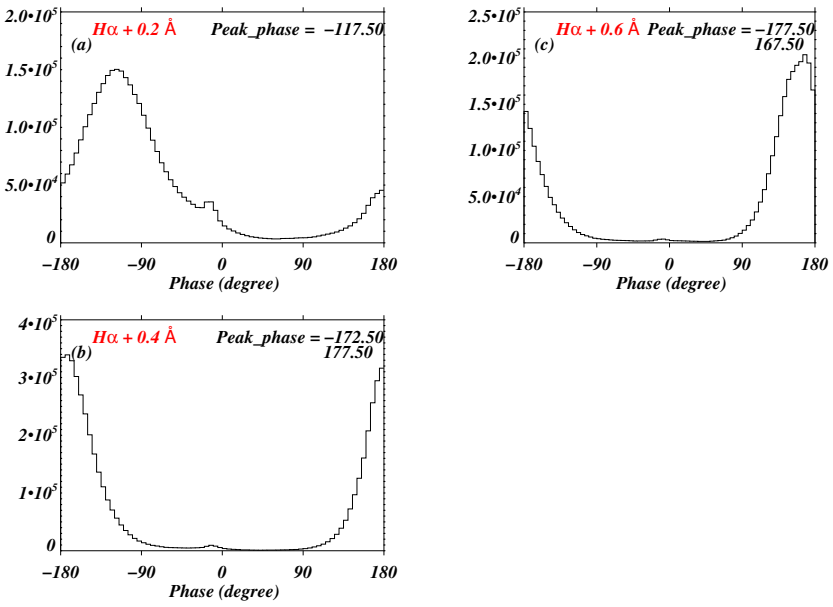

Figure 5.10: Panels (a)-(c) show the histogram of the significant phase differences extracted from all chosen locations in umbra between the intensity time-series derived from the blue wings of the Hα and the velocity time-series estimated using the Hα line profiles. Here, we have also mentioned the peak phase on each panel, similar to Figure 5.9.

various filters are shown in Figures 5.9 and 5.10. In Figure 5.9, panels (a)-(c) display the phase differences for the blue wings of Hα, while panel (d) shows those for the Hα core. Phase differences peak at -22.50° for Hα-0.2 Å, -7.50° for Hα-0.4 Å, and 7.50° for Hα-0.6 ÅḞor the Hα core, phase differences peak at -47.50°. In Figure 5.10, phase differences for the red wings of the Hα are presented. Across all panels, phase differences peak either around ±180° or around 0°. In the framework of linear MHD wave theory, oscillations in density (and consequently intensity) and velocity lasting several minutes are attributed to slow magnetoacoustic waves. The ideal phase relationships between intensity and velocity allow us to determine whether a slow wave is being propagated (either upward or downward) or is stationary. In-phase or out-of-phase variations are exhibited along the direction of propagation by propagating waves, while standing waves demonstrate a quarter-period variation in intensity and velocity (e.g., Kitagawa et al., 2010; Sangal et al., 2022; Wang et al., 2009a; Wang, 2011). In the blue wings of the Hα line, we observe in-phase variation between intensity and velocity, suggesting a connection to the upward propagation of the slow waves. Conversely, the red wings of the Hα line exhibit out-of-phase variation, indicating a link to the downward propagation of waves. It should be noted that the scanning steps from blue wing to red wing on each Hα line profiles takes some time steps. Therefore, this is obvious that we observe some distinct behaviour of wave propagation. In the subsequent Section 5.5, we provide interpretation of these results and emphasize their agreement with the chromospheric resonant cavity model.

5.5 Discussion and Conclusion

We utilized high-resolution observational data from the Big Bear Solar Observatory (BBSO) as observed by GST/VIS to investigate the oscillations within the umbral region of a highly magnetized sunspot. Our analysis focused on the intensity oscillations observed both at the core and the wings of the Hα line, along with the Doppler velocity estimated using various

the Hα line profiles. Through statistical analysis, we observed a prevalence of 3-minute oscillations in the chromospheric umbral region at multitude of locations. Moreover, our examination revealed the presence of both upward and downward propagating waves in the chromosphere, indicating that the distinct 3 minute umbral oscillations likely stem from the resonant modes within the sunspot. Resonance within the solar atmosphere appears to be the most plausible explanation for the observed oscillations in sunspots, as suggested by various studies (e.g., Zhugzhda and Locans, 1981). For resonances to occur within any atmospheric layer, waves must reflect from the boundaries of the layer.

A sunspot's umbral structure has a vertically stratified magnetic field, which allows for the confinement of several wave modes by the reflection. Umbral waves have characteristic periods of 3 and 5 minutes, indicating the presence of resonance modes. The chromospheric resonator, located in the cavity between the photosphere and the transition region of a sunspot, partially reflects slow magnetoacoustic waves, causing resonances (e.g., Zhugzhda, 2008, 2007). The steep temperature in the transition region forms a barrier that can reflect slow magnetoacoustic waves moving upward. These waves eventually reflected into the photosphere and are partly bounced back at the minimum temperature point, causing resonance within the chromospheric cavity. The main physical process in this scenario is partial reflection caused by temperature gradient in both the photosphere and the transition region, which facilitates the formation of resonances in the chromospheric cavity (e.g., Snow et al., 2015).

Zhugzhda and Locans (1981) and Zhugzhda et al. (1983) proposed that temperature gradients close to the photosphere's minimum temperature and the transition region are the source of high-frequency slow magneto-acoustic waves with 3 min periodicity that cause resonance in the chromosphere. The entire resonator is situated in a region with significant magnetic fields. It should be noted that the presently observed sunspot is strongly magnetized one. Many researchers followed this theory of the chromospheric

resonator. For instance, Locans et al. (1988) showed that the 2-3 min oscillations observed in sunspot umbrae are caused by slow magnetoacoustic waves that are partially restricted to the umbral photosphere and chromosphere. His understanding was achieved through numerical simulations using a semi-empirical model atmosphere. The chromospheric cavity oscillates at periods of around three minutes, according to Botha et al. (2011). These oscillations are able to travel upward into the corona because this cavity functions as a leaky resonator. In this chapter, we have also observed the existence of upward-traveling waves, resembling this leaky resonator behavior. Jess et al. (2020) proposed that the increased strength of umbral waves observed at chromospheric levels could be due to the presence of an acoustic resonator. They offered robust observational support for the existence of a resonance cavity above a sunspot with intense magnetic activity. They achieved this through a blend of techniques, including spectropolarimetric inversions and comparisons with detailed numerical simulations. The aurthor has proposed the presence of 3 min oscillation may not be necessary to explain the 3 min oscillations observed in the chromosphere and corona. In Figure 5.9, panels (a) to (c), the phase differences peak around 0°(i.e., in phase relationship), indicating the presence of upward propagating magnetoacoustic waves (e.g., Kitagawa et al., 2010; Sangal et al., 2022; Wang et al., 2009a; Wang, 2011). The blue wings, typically formed in the lower atmospheric layers (i.e., upper photosphere or lower chromosphere), show that these upward propagating waves move through the chromosphere. At the transition region boundary, these waves can partially reflect and transmit into the transition region and the corona. In panel (d) of Figure 5.9, the phase difference peaks at -47.5°, corresponding to the Hα core, which forms higher in the chromosphere. This value might result from the superposition of downward and upward propagating waves. For example, Gurman (1987) identified a phase difference of 77° when analyzing the relationship between velocity and intensity. They suggested that these variations result from the interaction of upward and downward moving waves with a

three-minute periodicity, indicating the presence of a chromospheric resonant cavity for acoustic waves within the sunspot umbra.

In Figure 5.10, across all panels (a)-(c), the phase difference consistently peaks around either 180° or -180°. An out-of-phase relationship between intensity and velocity signals indicates the presence of downward propagating waves (Wang et al., 2009a). In our analysis, this pattern corresponds to the red wings of the Hα. The red wings form at higher heights compared to the blue wings, primarily due to velocity differences: the blue wing forms at slightly lower heights due to upflows, while the red wing forms at slightly higher heights due to downflows (e.g., White and Wilson, 1966; Zelenka, 1975). Consequently, we observe signatures of downward propagating waves at the red wings, as evidenced by the phase difference peaking at out-of-phase values (+180° or -180°).

We found that current observations support with a chromospheric resonator over sunspot umbrae. The observed data, when analysed, reveal strong 3-minute power spectrum oscillations above the sunspot umbra. Since the chromospheric resonator is a partial resonator, oscillations will occasionally escape into the corona and propagate into the solar atmosphere at the transition region. In different solar region, we can discover the characteristics of magnetohydrodynamic (MHD) waves in order to learn more about their drivers and the processes that transport energy from the lower atmospheric layers into the corona. This investigation may yield important clues regarding the contribution of these waves to the process of coronal heating.